Inverted heterojunction solar cells incorporating fullerene/polythiophene composite core/shell nanorod arrays



2010 Nanotechnology 21 145203

(http://iopscience.iop.org/0957-4484/21/14/145203)

Nanotechnology **21** (2010) 145203 (8pp) doi:10.1088/0957-4484/21/14/145203

# Inverted heterojunction solar cells incorporating fullerene/polythiophene composite core/shell nanorod arrays

**Hsu-Shen Wang[1], Shih-Yung Chen[2], Ming-Hsin Su[1], Yuh-Lin Wang[2,3] and Kung-Hwa Wei[1]**

[1] Department of Materials Science and Engineering, National Chiao Tung University, 1001 Ta Hsueh Road, Hsinchu 30050, Taiwan, Republic of China
[2] Institute of Atomic and Molecular Science, Academia Sinica, PO Box 23-166, Taipei 106, Taiwan, Republic of China
[3] Department of Physics, National Taiwan University, Taipei 106, Taiwan, Republic of China

E-mail: khwei@mail.nctu.edu.tw

Received 31 December 2009, in final form 20 February 2010
Published 11 March 2010
Online at stacks.iop.org/Nano/21/145203

**Abstract**

We have fabricated inverted heterojunction solar cell devices incorporating [6,6]-phenyl-$C_{61}$-butyric acid methyl ester/poly(3-hexylthiophene) core/shell nanorod arrays by using an anodic alumina oxide template. The internal quantum efficiencies and external quantum efficiencies of these core/shell nanorod inverted solar cells were higher than those of the corresponding conventional inverted bulk heterojunction device. The optimized nanorod array structure had a high hole mobility that was over one order magnitude greater than that of the conventional bulk heterojunction structure, as determined by fitting the dark $J$–$V$ curves into the space charge limited current model. The more efficient carrier transport of the device incorporating the core/shell nanorod arrays provided it with both a higher short-circuit current density and power conversion efficiency.

(Some figures in this article are in colour only in the electronic version)

## 1. Introduction

The development of conjugated polymers for use in organic optoelectronic devices is an active field of research. In particular, polymer heterojunction solar cells have attracted much attention because of their potential application in large-area, flexible, low-cost devices [1–8]. The power conversion efficiencies (PCEs) of bulk heterojunction (BHJ) solar cells have improved dramatically over the last few years. For example, the PCEs of BHJ solar cells, incorporating regioregular poly(3-hexylthiophene) (P3HT) as the donor and [6,6]-phenyl-$C_{61}$-butyric acid methyl ester (PCBM) as the acceptor, have recently reached values of ca. 4–5% under standard solar conditions (AM 1.5 G, 100 mW cm$^{-2}$) [9–14]. Nevertheless, the PCEs of these polymer BHJ devices must improve further if they are to be employed practically, necessitating the development of unconventional structures. Alternating donor and acceptor phases possessing vertically aligned geometries, such as alternating nanorods, appear to be ideal structures for independent carrier transport [15, 16]. These structures are, however, difficult to obtain because of the complexity of the fabrication tools available. For the production of ordered polymeric nanorod arrays, template based approaches are probably most suitable.

Inverted BHJ devices incorporating metal oxides [17–21] such as $TiO_x$ and $MoO_3$ as electrodes and high-work-function anodes (e.g., Ag and Au) have been developed recently to avoid the problems of oxidation [22, 23], which occurs in low-work-function cathodes, and degradation of the indium tin oxide (ITO)–poly(ethylenedioxythiophene) (PEDOT) interface, which occurs frequently in conventional solar cell structures. In this study, we use core/shell-structured PCBM/P3HT nanorod arrays as the active layer, which we fabricated using an anodic aluminum oxide (AAO) membrane, to construct an inverted solar cell. To the best of our knowledge, this is the first report of PCBM/P3HT nanorod arrays being incorporated into inverted BHJ solar cells. Our approach has several advantageous features (figure 1):

 

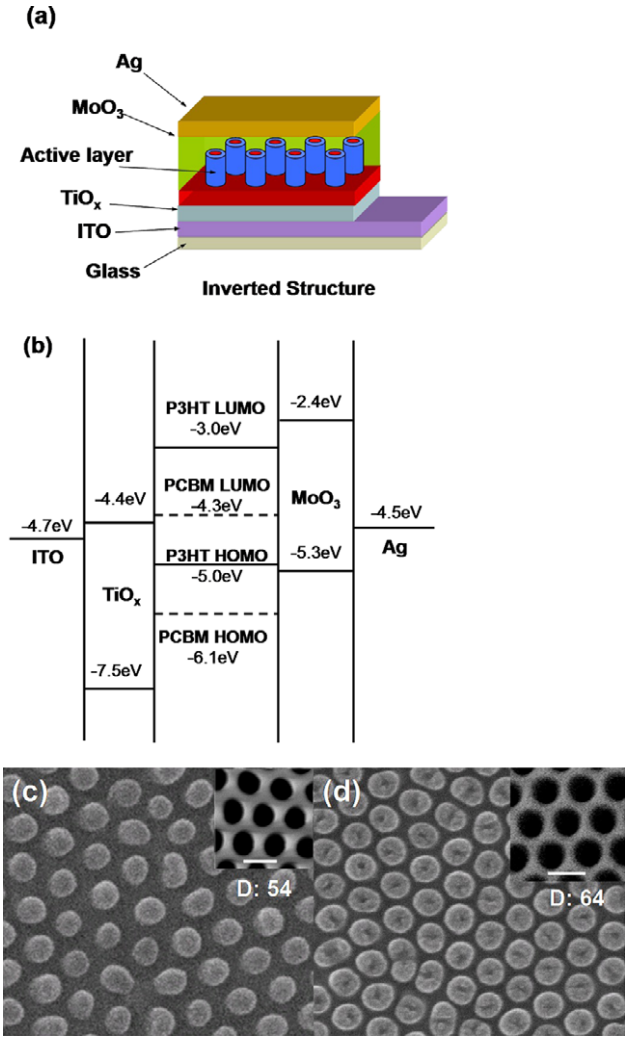


**Figure 1.** (a) Schematic representations of the inverted structure and the PCBM/P3HT core/shell structure of the inverted solar cell device. (b) Energy level diagram of the inverted solar cell device. Also, SEM images of PCBM/P3HT (1:1, w/w) nanorod arrays featuring nanorods having diameters and covered densities ($D$) on the substrate of (c) 70 nm and 54%, (d) 80 nm and 64%, respectively. (Figures A.1 and A.2 show the large area and cross-sectional images of the nanorods).

(i) the energy level of the highest occupied molecular orbital (HOMO) of the shell (P3HT-rich region) can match that of the metal oxide electrode deposited for hole transport on the shell; (ii) the energy level of the lowest unoccupied molecular orbital (LUMO) of the core (PCBM-rich region) can also match that of the other metal oxide layer for the transport of electrons; and (iii) the direct transport of holes and electrons along the phase-separated shell and core, respectively, occurs in the nanorods. Hence, we expected that such core/shell nanorod array devices featuring a high covered density of nanorods on the substrate and an inverted device geometry would provide more efficient devices.

## 2. Experimental section

Regioregular P3HT (4002-E, Rieke Metals), PCBM (Nano-C, Inc.), and poly(3,4-ethylenedioxythiophene:polystyrenesulfonate) (PEDOT:PSS) (Baytron P VP Al 4083, Inc.) were obtained commercially.

A solution of titanium isopropoxide (Alfa, 99.995%; 10 wt%) in isopropyl alcohol was spin-coated onto pre-cleaned ITO glass substrates under a $N_2$ ambient and was then converted to 40 nm thick $TiO_x$ via hydrolysis at room temperature in air for 2 h. The substrate was then heated at 450 °C for 30 min to complete the hydrolysis reaction.

PCBM/P3HT films of various thicknesses were prepared through solution casting onto ITO/$TiO_x$ substrates; an AAO membrane was then placed on top of the PCBM/P3HT films. This PCBM:P3HT film/AAO membrane was sandwiched between two glass slides and then placed in an oven and annealed at 120 °C under vacuum. After 6 h, the assembled system was cooled to room temperature. Dissolving the alumina membranes in 10 wt% NaOH solution released the PCBM/P3HT core/shell nanorod structures, which were dried under vacuum for 12 h prior to characterization. SEM images of the resultant PCBM/P3HT nanostructures were recorded using a JEOL 6500 scanning electron microscope operated at an accelerating voltage of 15 kV. The samples were coated with a thin (ca. 3 nm) layer of Pt prior to SEM imaging.

The current density–voltage ($J$–$V$) characteristics of the polymers were measured using devices having the structure ITO/$TiO_x$/PCBM:P3HT/$MoO_3$/Ag. The ITO-coated glass substrate was pre-cleaned and treated with oxygen plasma prior to use. The $TiO_x$ layer was prepared using the spin-coating process described above. The PCBM/P3HT layer was spin-coated from a chlorobenzene solution. Using a base pressure of less than $1 \times 10^{-6}$ Torr, layers of $MoO_3$ (20 nm) and Ag (80 nm) were vacuum deposited to form the anode.

The devices were tested under simulated AM 1.5 G irradiation (100 mW cm$^{-2}$) using a Xe lamp based Newport 66902 150 W solar simulator equipped with an AM1.5 filter as the white light source; the optical power at the sample was 100 mW cm$^{-2}$, detected using an OPHIR thermopile 71964. The $J$–$V$ characteristics were measured using a Keithley 236 source-measure unit. The EQEs were measured using a Keithley 236 source-measure unit coupled with an Oriel Cornerstone 130 monochromator. The light intensity at each wavelength was calibrated using an OPHIR 71580 diode.

The hole-only samples, used to investigate hole transport in the polymer/PCBM layers, were fabricated with the structure of a ITO/PEDOT/nanorod array. The $J$–$V$ curves was measured by conductive atomic force microscopy (C-AFM) using platinum-coated silicon cantilevers (NanoSensors Inc. (PPP-ContPt, spring constant $k = 0.2$ N m$^{-1}$), tip diameter ~20 nm) and a Digital Nanoscope IV operated under ambient conditions. For $J$–$V$ measurement of C-AFM, we determined the contact area between the tip and sample assuming a 20 nm diameter circle. The $J$–$V$ curves from each sample were averaged from four different regions.

## 3. Result and discussion

Figures 1(a) and (b) provide a schematic representation of the PCBM/P3HT core/shell nanorod arrays in an inverted solar cell structure and an energy level diagram for each material,

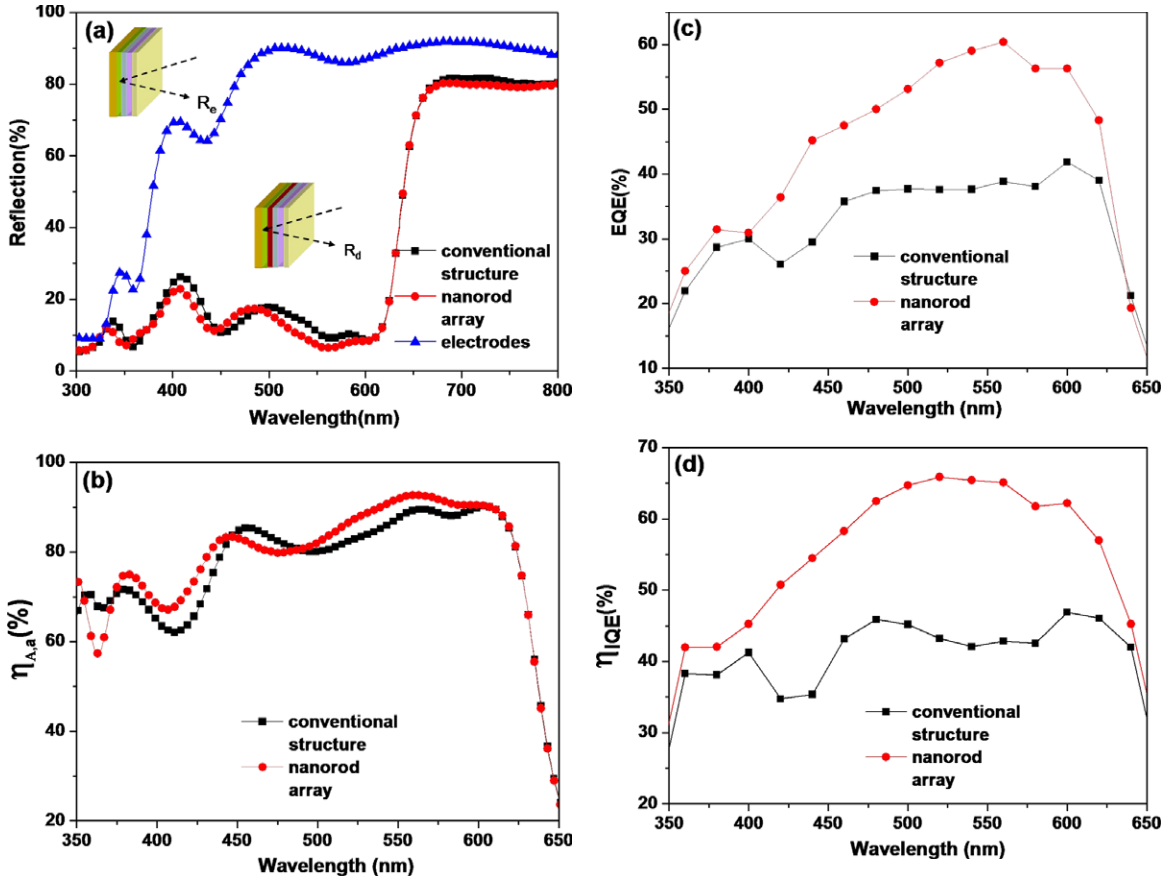


**Figure 2.** (a) Reflectance spectra of PCBM/P3HT nanorod array BHJ solar cell devices (conventional structure; nanorod array) and of the electrodes. Device structure: glass/ITO (250 nm)/$TiO_x$ (45 nm)/nanorod array (200 nm long, 80 nm diameter)/$MoO_3$ (20 nm)/Ag (80 nm); sample only with electrodes: a device fabricated without the active layer. Inset: schematic representation of the incident light path in a completed device and sample only with electrodes. (b) Absorption efficiency ($\eta_{A,a}$) of the devices. (c) EQE spectra of the nanorod array inverted devices and the conventional structure inverted devices. (d) Internal quantum efficiency ($\eta_{IQE}$) spectra of PCBM/P3HT BHJ solar cells (conventional structure; nanorod array with diameter: 80 nm; length: 200 nm).

respectively. In this nanorod based inverted architecture, we positioned a $TiO_x$ layer between the ITO glass and the active layer because it is an appropriate material for the electron-collecting ITO/$TiO_x$ bottom electrode. The energy level of the LUMO of $TiO_x$ is −4.4 eV, which suggests that electrons (LUMO of PCBM: −4.3 eV) can be injected into the $TiO_x$ interlayer, while the holes from the active layer blend levels can be effectively blocked (HOMO of $TiO_x$: −7.5 eV). The thickness of the $TiO_x$ thin film was 45 nm; its root-mean-square (RMS) roughness, determined through atomic force microscopic analysis, was 1.2 nm (see appendix figure A.3). In this study, the configuration of the device, stacked from bottom to top, was ITO/$TiO_x$/PCBM:P3HT (0.8:1, w/w) nanorod arrays/$MoO_3$/Ag. Here, the hole transport layer ($MoO_3$) was deposited on the shell (p-type rich region) of the nanorods as a hole-selecting layer.

Figures 1(c) and (d) display scanning electron microscopy (SEM) images of the PCBM/P3HT (1:1, w/w) nanorod array structure with 54% and 64% covered density, determined by pore size of AAO template (70 and 80 nm) on the substrate. The average diameter of the nanorods was equal to the diameter of the nanopores in the ordered AAO template, revealing our good control over the nanorod diameter. We used melt-assisted wetting of ordered AAO templates to fabricate the PCBM/P3HT core/shell nanorod (core: PCBM-rich region; shell: P3HT-rich region) structure. The phase separation of the PCBM/P3HT blends during the wetting of the porous AAO membrane was determined by the flow-induced shear stress, and its mechanism was described in a previous report [16].

Figure 2(a) displays the reflectance spectra of the PCBM/P3HT nanorod array solar cell device and of the device formed without the active layer. The actual amount of the light absorbed in each device ($A$) can be estimated by deducting the reflectance in the device ($R$) from the intensity of incident light ($A = 1 - R$), because the metal electrodes ($MoO_3$/Ag) of the devices did not allow any transmission of incident light. The absorption efficiency in the active layer $\eta_{A,a}$ was determined [24] from the light absorbed in the photoactive layer ($A_a$), and reflectances of the device ($R_d$) and the electrodes ($R_e$):

$$\eta_{A,a} = 1 - \frac{R_d}{R_e}. \quad (1)$$

For the control experiment, we employed a conventional BHJ device having an active layer thickness that was the same

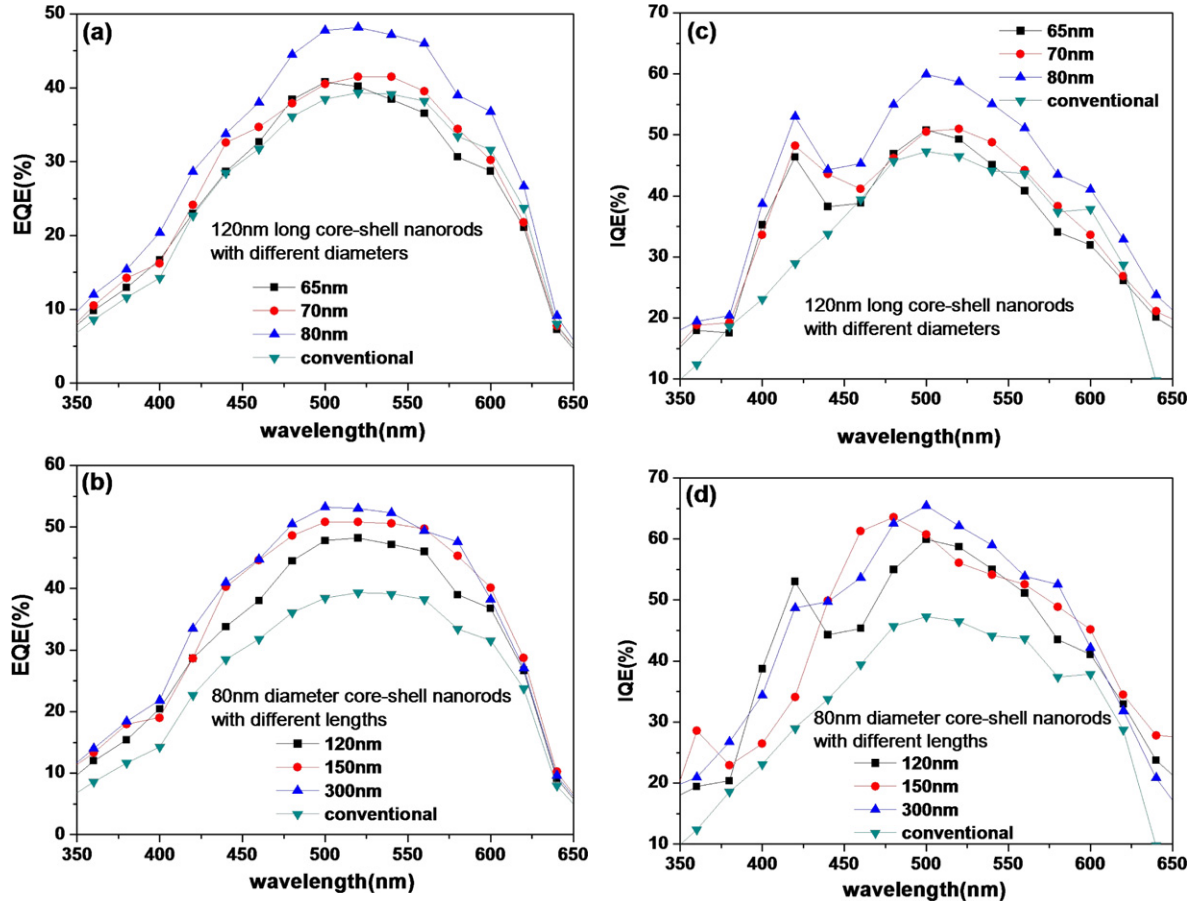


**Figure 3.** (a) The EQEs of 120 nm length nanorods with diameters of 65, 70 or 80 nm. (b) The EQEs of 80 nm diameter nanorods with lengths of 120, 150 or 300 nm. (c) The IQEs of 120 nm length nanorods with diameters of 65, 70 or 80 nm. (d) The IQEs of 80 nm diameter nanorods with lengths of 120, 150 or 300 nm. (Figure A.4 shows the correlated reflectance spectra and absorption efficiency spectra of EQEs and IQEs).

as the length of the nanorods. The nanorod arrays having a diameter of 80 nm and a length of 200 nm exhibited a reflection intensity that was lower than that of the conventional device.

Figure 2(b) displays the absorption efficiencies of the devices. Even though it featured a smaller absorption area, associated with the gaps between the nanorods, our nanorod array based device exhibited superior absorption efficiency relative to that of the conventional BHJ structure.

Figure 2(c) presents the external quantum efficiencies (EQEs) of PCBM/P3HT nanorod array devices. The nanorod array device structure provided higher EQEs in the region from 420 to 600 nm than did the conventional device; e.g., at 520 nm, they were 57% and 37%, respectively. Therefore, we expected most of the electron/hole pairs to separate efficiently at the p–n interface, such that electron and hole transport would occur through the PCBM-rich (n-type) and P3HT-rich (p-type) regions, respectively.

Figure 2(d) displays the internal quantum efficiency (IQE) spectra of the devices; the values of $\eta_{\mathrm{IQE}}$ were obtained using the equation

$$\eta_{\mathrm{IQE}} = \frac{\eta_{\mathrm{EQE}}}{\eta_{A,\mathrm{a}}}. \qquad (2)$$

The device featuring the nanorod arrays exhibited enhanced IQEs at wavelengths in the region 440–620 nm, due to their more efficient charge carrier transport, relative to those of the conventional inverted device; e.g., the IQEs at 520 nm were 66 and 43%, respectively.

Figure 3 reveals the EQEs and IQEs of devices with different nanorod dimensions without annealing. Figure 3(a) shows that at 520 nm wavelength the EQE increased to 48% for 80 nm diameter nanorods from 40% for 65 nm diameter nanorods at a fixed nanorod length of 120 nm. Figure 3(b) shows the EQE value increased to 53% for 300 nm length nanorods from 48% for 120 nm length nanorods at a fixed diameter of 80 nm. Whereas, figure 3(c) shows that at 520 nm wavelength the IQE increased to 59% for 80 nm diameter nanorods from 49% for 65 nm diameter nanorods at a fixed nanorod length of 120 nm. Figure 3(d) shows the IQE increased to 62% for 300 nm length nanorods from 59% for 120 nm length nanorods at a fixed nanorod diameter of 80 nm. Table 1 summarizes the EQEs and IQEs of the devices with various nanorod dimensions. The increase in IQEs of these nanorod devices can be reasonably assumed by the fact that their rod structure facilitates the charge transport, as opposed to the case in the conventional device structure. This requires further investigation of their transport properties. We used conductive atomic force microscopy rather than using a sandwiched device structure because the active layer are not

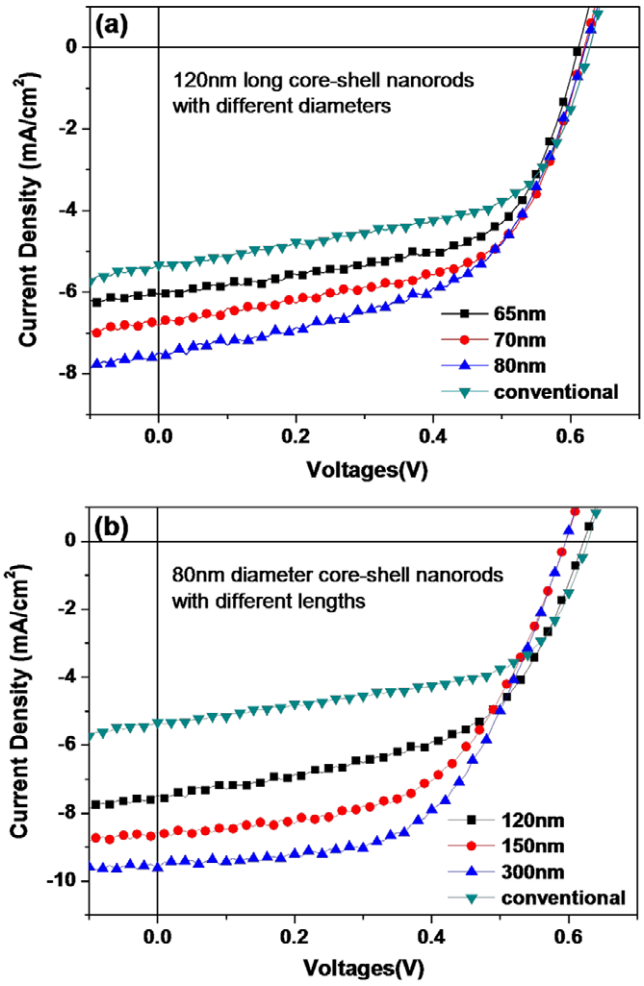


**Figure 4.** (a) $J$–$V$ characteristics of PCBM/P3HT nanorod array devices incorporating 120 nm length nanorods with diameters of 65, 70 and 80 nm. (b) $J$–$V$ characteristics of PCBM/P3HT nanorod array devices incorporating 80 nm diameter nanorods having lengths of 120, 150, and 300 nm. Devices were measured under AM 1.5 G illumination at an intensity of 100 mW cm$^{-2}$. The thickness of the active layer for conventional structure is 120 nm.

**Table 1.** External quantum efficiencies (EQEs) and internal quantum efficiencies (IQEs) at 520 nm from nanorods of various sizes.

| Pore size (nm) | Length (nm) | EQE (%) | IQE (%) |
|---|---|---|---|
| Conventional | — | 39 | 47 |
| 65 | 120 | 40 | 49 |
| 70 | 120 | 42 | 51 |
| 80 | 120 | 48 | 59 |
| 80 | 150 | 51 | 56 |
| 80 | 200 | 57 | 66 |
| 80 | 300 | 53 | 62 |

planar; depositing a thin layer of electrode would cause an uneven conducting path.

Figure 4 displays the $J$–$V$ characteristics of solar cell devices incorporating different nanorod dimensions without annealing. Figure 4(a) shows that the short current densities ($J_{sc}$) and power conversion efficient (PCE) increased to

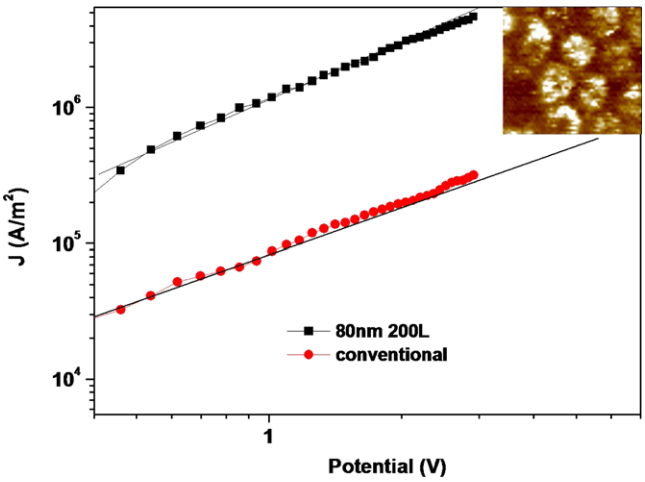


**Figure 5.** Conducting atomic force microscopy (C-AFM) dark $J$–$V$ curves for hole-dominated carrier samples incorporating PCBM/P3HT (0.8:1, w/w) in conventional structure and nanorod array structures. Inset: C-AFM current images of PCBM/P3HT nanorods.

**Table 2.** Electronic parameters of vertical p–n junction devices prepared from nanorods of various sizes. (Note: active layer: PCBM/P3HT (0.8:1, w/w).)

| Pore size | Length (nm) | $J_{sc}$ [a] (mA cm$^{-2}$) | $V_{oc}$ [b] (V) | FF [c] (%) | $\eta$ [d] (%) |
|---|---|---|---|---|---|
| Conventional | — | 5.33 | 0.63 | 56.6 | 1.90 |
| 65 | 120 | 6.05 | 0.61 | 59.1 | 2.18 |
| 70 | 120 | 6.82 | 0.62 | 57.2 | 2.43 |
| 80 | 120 | 7.48 | 0.62 | 53.9 | 2.50 |
| 80 | 150 | 8.54 | 0.60 | 55.1 | 2.82 |
| 80 | 200 | 9.44 | 0.59 | 58.4 | 3.25 |
| 80 | 300 | 9.61 | 0.60 | 55.5 | 3.20 |

[a] Short-circuit current density. [b] Open circuit voltage.
[c] Fill factor. [d] Power conversion efficiency.

7.5 mA cm$^{-2}$ and 2.5%, respectively, for 80 nm diameter nanorods from 6.1 mA cm$^{-2}$ and 2.2% for 65 nm diameter nanorods at a fixed nanorod length of 120 nm. Figure 4(b) shows the $J_{sc}$ and PCE increased to 9.6 mA cm$^{-2}$ and 3.2%, respectively, for 300 nm length nanorods from 7.5 mA cm$^{-2}$ and 2.5% for 120 nm length nanorods at a fixed diameter of 80 nm. This shows that the devices with longer and larger nanorods result in higher power conversion efficiency. Table 2 summarizes the performance factors of the devices with different nanorod dimensions without annealing.

Figure 5 presents the dark $J$–$V$ curves by hole-dominated conductive atomic force microscopy measurement. We determined the hole mobilities by fitting the dark $J$–$V$ curves into the space charge limited current (SCLC) model using the equation

$$J = 9\varepsilon_o\varepsilon_r\mu_h V^2/8L^3 \quad (3)$$

where $\varepsilon_o$ is the permittivity of free space, $\varepsilon_r$ is the dielectric constant of the polymer, $\mu_h$ is the hole mobility, $V$ is the voltage drop across the device, and $L$ is the polymer thickness [25, 26]. The PCBM/P3HT (0.8:1, w/w)

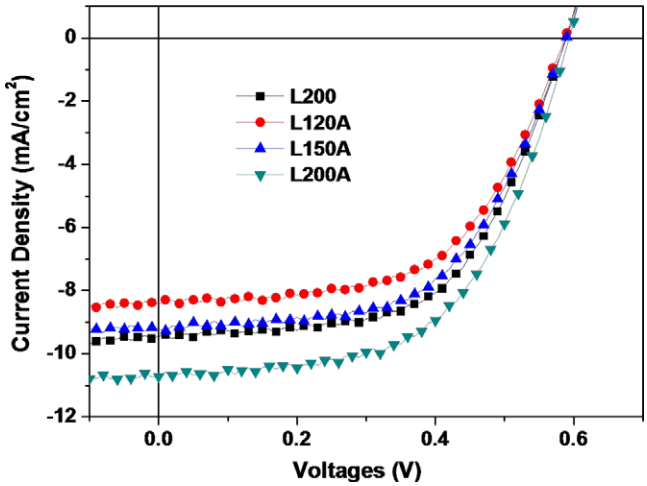


**Figure 6.** $J$–$V$ characteristics of annealed PCBM/P3HT nanorod array devices incorporating 80 nm diameter nanorods having lengths of 120, 150, and 200 nm. Devices were annealed at 120 °C for 10 min and then measured under AM 1.5 G illumination at an intensity of 100 mW cm$^{-2}$.

nanorod array structure exhibited a hole mobility ($5.98 \times 10^{-4}$ cm$^2$ V$^{-1}$ s$^{-1}$) that was relative greater than that ($4.73 \times 10^{-5}$ cm$^2$ V$^{-1}$ s$^{-1}$) of the conventional BHJ structure. The device featuring the 80 nm diameter, 200 nm long core/shell nanorod arrays exhibited a higher mobility of $5.98 \times 10^{-4}$ cm$^2$ V$^{-1}$ s$^{-1}$ along the out-of-plane direction, indicating that the P3HT-rich shell on these nanorods facilitated hole transport, even though a small amount of PCBM was quite possibly present in the P3HT-rich shell. We believe that the increase in hole mobility was due to the phase separation in the core/shell nanorod structure and the increased crystallinity [16] of P3HT in the P3HT-rich shells, caused by the much lower PCBM concentration than that found in the active P3HT/PCBM layers in conventional BHJ devices.

Further improvement on the PCE of the devices with nanorod structures can be carried out by annealing. Figure 6 displays the $J$–$V$ characteristics of solar cell devices incorporating the annealed PCBM/P3HT nanorod arrays. The short current densities ($J_{sc}$) and the PCEs both increased after annealed at 120 °C for 10 min; e.g., the annealed device increased to 10.7 mA cm$^{-2}$ and 3.6%, respectively, from 9.4 mA cm$^{-2}$ and 3.3%, for the pristine device with the 200 nm nanorod. Table 3 summarizes the performance factors of the various devices. We suspect that the improved performance after annealing resulted from improved contact at the electrodes, allowing more efficient transfer of holes and electrons, and also from increases in the degree of polymer crystallization [11] and the transport efficiency of the P3HT-rich region.

## 4. Conclusion

In conclusion, we have fabricated inverted BHJ solar cell devices incorporating PCBM/P3HT core/shell nanorod arrays. As a result of superior carrier transport, the internal and external quantum efficiencies of these core/shell nanorod inverted solar cells were both higher than those of the corresponding conventional inverted BHJ device. The optimized nanorod array structure had a high hole mobility that was over one order magnitude greater than that of the conventional BHJ structure, as determined by fitting the dark $J$–$V$ curves into the space charge limited current model; the corresponding device displayed more efficient carrier transport, which contributed to a higher short-circuit current density and PCE, relative to those of the conventional device.

**Table 3.** Electronic parameters of vertical p–n junction devices prepared from nanorods of various sizes. (Note: active layer: PCBM/P3HT (0.8:1, w/w).)

| Pore size | Length (nm) | $J_{sc}$ [a] (mA cm$^{-2}$) | $V_{oc}$ [b] (V) | FF [c] (%) | $\eta$ [d] (%) | Annealing temperature [e] (°C) |
|---|---|---|---|---|---|---|
| 80 | 120 | 7.48 | 0.62 | 53.9 | 2.50 | — |
| 80 | 120 | 8.43 | 0.59 | 57.1 | 2.83 | 120 |
| 80 | 150 | 9.21 | 0.59 | 56.8 | 3.08 | 120 |
| 80 | 200 | 10.70 | 0.59 | 56.8 | 3.60 | 120 |

[a] Short-circuit current density. [b] Open circuit voltage.
[c] Fill factor. [d] Power conversion efficiency.
[e] Annealing time: 10 min.

## Acknowledgments

We are grateful for the financial support provided by the National Science Council through Project NSC 97-2120-M-009-006. We thank Professor Tzung-Fang Guo for discussion of device fabrication.

## Appendix

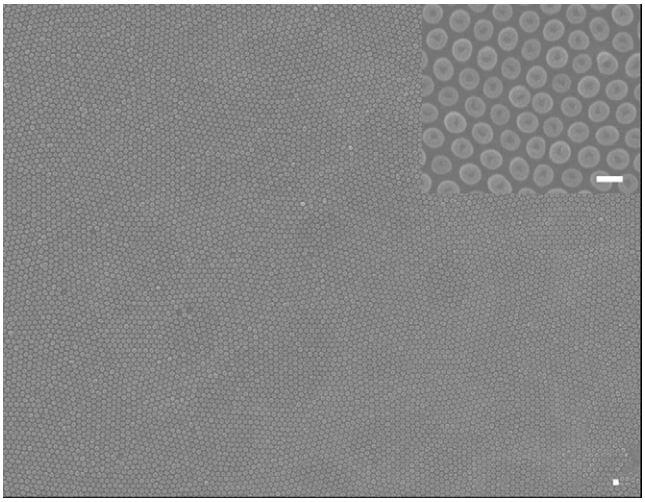

**Figure A.1.** Large-area SEM image of the PCBM/P3HT (1:1, w/w) nanorod array; inset: magnified image (scale bar: 100 nm).

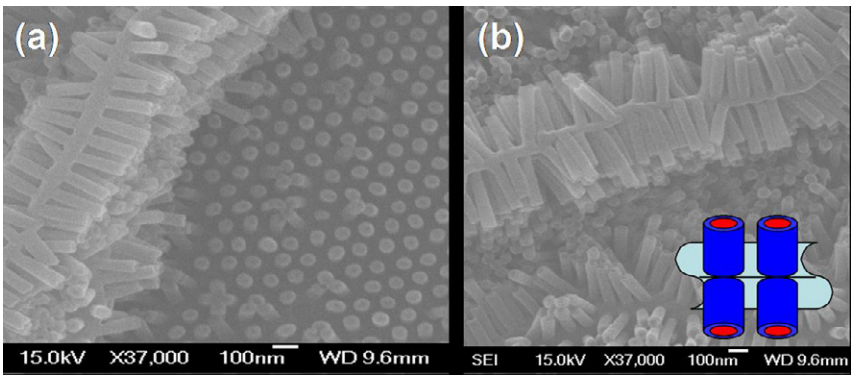


**Figure A.2.** SEM images of PCBM/P3HT (1:1, w/w) nanorod arrays having lengths of (a) 200 and (b) 300 nm. Inset to (b): cartoon representation of the structure in the cross-sectional image.

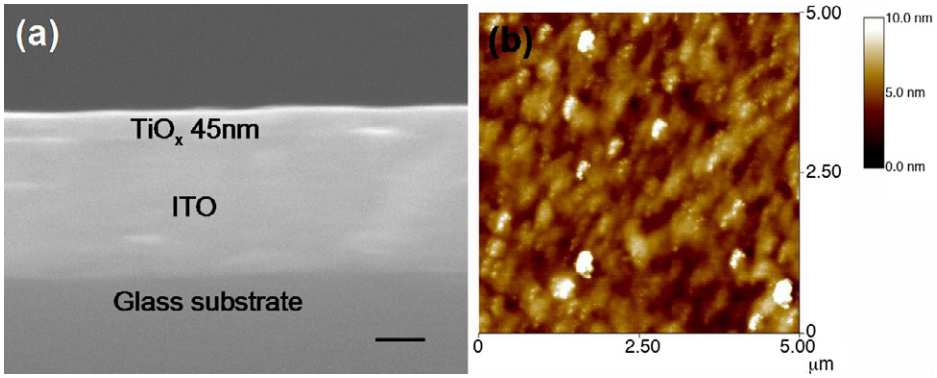


**Figure A.3.** (a) Cross-sectional SEM image of ITO glass/$TiO_x$; the thickness of the $TiO_x$ layer was 45 nm. (b) AFM image of glass/$TiO_x$ surface; the RMS roughness of this film was 1.2 nm.

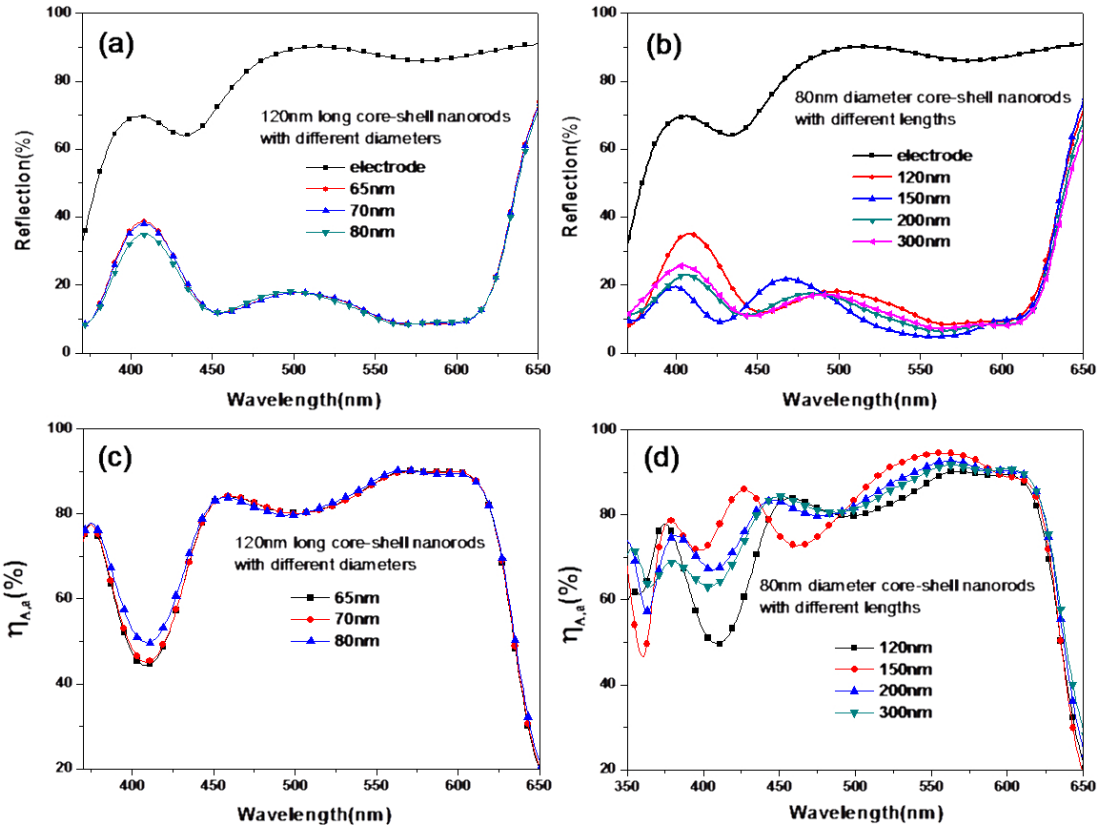


**Figure A.4.** (a) and (b) Reflectance spectra of PCBM/P3HT nanorod array, with different diameters (65–80 nm) and length (120–300 nm) respectively, solar cell devices. (c) and (d) Absorption efficiency ($\eta_{A,a}$) of the devices with different diameters and lengths, respectively.

## References


[1] Yu G, Gao J, Hummelen J C, Wudl F and Heeger A J 1995 *Science* **270** 1789

[2] Park S H, Roy A, Beaupre S, Cho S, Coates N, Moon J S, Moses D, Leclerc M, Lee K and Heeger A J 2009 *Nat. Photon.* **3** 297

[3] Lin Y Y, Wang D Y, Yen H C, Chen H L, Chen C C, Chen C M, Tang C Y and Chen C W 2009 *Nanotechnology* **20** 405207

[4] Chang Y T, Hsu S L, Su M H and Wei K H 2009 *Adv. Mater.* **21** 2093

[5] Dridi C, Barlier V, Chaabane H, Davenas J and Ouada H B 2008 *Nanotechnology* **19** 375201

[6] Peet J, Senatore M L, Heeger A J and Bazan G C 2009 *Adv. Mater.* **21** 1521

[7] Oey C C, Djurisic A B, Wang H, Man K K Y, Chan W K, Xie M H, Leung Y H, Pandey A, Nunzi J M and Chui P C 2006 *Nanotechnology* **17** 706

[8] Yu B Y, Tsai A, Tsai S P, Wong K T, Yang Y, Chu C W and Shyue J J 2008 *Nanotechnology* **19** 255202

[9] Kumar A, Li G, Hong Z and Yang Y 2009 *Nanotechnology* **20** 165202

[10] Hadipour A, Boer B D and Blom P W M 2008 *Adv. Funct. Mater.* **18** 169

[11] Chiu M Y, Jeng U S, Su C H, Liang K S and Wei K H 2008 *Adv. Mater.* **20** 2573

[12] Chen L M, Hong Z, Li G and Yang Y 2009 *Adv. Mater.* **21** 1434

[13] Dennler G, Scharber M C and Brabec C J 2009 *Adv. Mater.* **21** 1323

[14] Li G, Shrotriya V, Huang J, Yao Y, Moriarty T, Emery K and Yang Y 2005 *Nat. Mater.* **4** 864

[15] Mayer A C, Scully S R, Hardin B E, Rowell M W and McGehee M D 2007 *Mater. Today* **10** 28

[16] Wang H S, Lin L H, Chen S Y, Wang Y L and Wei K H 2009 *Nanotechnology* **20** 075201

[17] Waldauf C, Morana M, Denk P, Schilinsky P, Coakley K, Choulis S A and Brabec C J 2006 *Appl. Phys. Lett.* **89** 233517

[18] White M S, Olson D C, Shaheen S E, Kopidakis N and Ginley D S 2006 *Appl. Phys. Lett.* **89** 143517

[19] Xu Z, Chen L M, Yang G, Huang C H, Hou J, Wu Y, Li G, Hsu C S and Yang Y 2009 *Adv. Funct. Mater.* **19** 1227

[20] Kyaw A K K, Sun X W, Jiang C Y, Lo G Q, Zhao D W and Kwong D L 2008 *Appl. Phys. Lett.* **93** 221107

[21] Schmidt H, Flügge H, Winkler T, Bülow T, Ried T and Kowalsky W 2009 *Appl. Phys. Lett.* **94** 243302

[22] de Jong M P, van Ijzendoorn L J and de Voigt M J A 2006 *Appl. Phys. Lett.* **77** 2255

[23] Wong K W, Yip H L, Luo Y, Wong K Y, Laua W M, Low K H, Chow H F, Gao Z Q, Yeung W L and Chang C C 2006 *Appl. Phys. Lett.* **80** 2788

[24] Jo J, Na S I, Kim S S, Lee T W, Chung Y, Kang S J, Vak D and Kim D Y 2009 *Adv. Funct. Mater.* **19** 2398

[25] Melzer C, Koop E J, Mihailetchi V D and Blom P W M 2004 *Adv. Funct. Mater.* **14** 865

[26] Mihailetchi V D, Koster L J A, Blom P W M, Melzer C, Boer B de, Duren J K J van and Janssen R A J 2005 *Adv. Funct. Mater.* **15** 795